Bioactive Materials 25 (2023) 319–332

Contents lists available at ScienceDirect

Bioactive Materials

journal homepage: www.keaipublishing.com/en/journals/bioactive-materials

Multi-layer-structured bioactive glass nanopowder for multistage-stimulated hemostasis and wound repair

Yidan Wang [a,b,1], Meng luo [a,b,1], Ting Li [a,b], Chenxi Xie [a,b], Sihua Li [a,b], Bo Lei [a,b,c,d,*]

[a] Frontier Institute of Science and Technology, Xi'an Jiaotong University, Xi'an, 710054, China
[b] Key Laboratory of Shaanxi Province for Craniofacial Precision Medicine Research, College of Stomatology, Xi'an Jiaotong University, Xi'an, 710054, China
[c] State Key Laboratory for Mechanical Behavior of Materials, Xi'an Jiaotong University, Xi'an, 710054, China
[d] Instrument Analysis Center, Xi'an Jiaotong University, Xi'an, 710054, China

ARTICLE INFO

Keywords:
Bioactive materials
Bioceramics
Bioactive glass nanoparticles
Wound repair

ABSTRACT

Current treatments for full-thickness skin injuries are still unsatisfactory due to the lack of hierarchically stimulated dressings that can integrate the rapid hemostasis, inflammation regulation, and skin tissue remodeling into the one system instead of single-stage boosting. In this work, a multilayer-structured bioactive glass nanopowder (BGN@PTE) is developed by coating the poly-tannic acid and ε-polylysine onto the BGN *via* facile layer-by-layer assembly as an integrative and multilevel dressing for the sequential management of wounds. In comparison to BGN and poly-tannic acid coated BGN, BGN@PTE exhibited the better hemostatic performance because of its multiple dependent approaches to induce the platelet adhesion/activation, red blood cells (RBCs) aggregation and fibrin network formation. Simultaneously, the bioactive ions from BGN facilitate the regulation of the inflammatory response while the poly-tannic acid and antibacterial ε-polylysine prevent the wound infection, promoting the wound healing during the inflammatory stage. In addition, BGN@PTE can serve as a reactive oxygen species scavenger, alleviate the oxidation stress in wound injury, induce the cell migration and angiogenesis, and promote the proliferation stage of wound repair. Therefore, BGN@PTE demonstrated the significantly higher wound repair capacity than the commercial bioglass dressing Dermlin™. This multifunctional BGN@PTE is a potentially valuable dressing for full-thickness wound management and may be expected to extend to the other wounds therapy.

1. Introduction

Skin wound healing is a highly coordinated and spatiotemporally regulated process that involves a multistep progression of the four distinct yet overlapping stages including hemostasis, inflammation, proliferation, and remodeling [1]. The hemostatic response is the first step in dealing with skin tissue injury and can encourage the development of subsequent biological events, such as supporting immune responses and wound healing [2,3]. Moreover, the blood clots provide a viable dynamic matrix for incoming inflammatory cells, fibroblasts, which were involved in the later stages of tissue repair [4,5]. In addition, the overproduction of reactive oxygen species (ROS) during wound infection stimulated the secretion of a large number of inflammatory mediators in the wound site microenvironment that allowed the wound to enter into a persistent inflammatory phase, thereby hindering wound healing [6,7]. The optimal state of wound healing mainly relies on an appropriate inflammatory level. The previous study demonstrated that ceria nanocrystals decorated mesoporous silica nanoparticles can restrict ROS exacerbation-mediated damage and suppress the inflammatory response to facilitate the wound healing process [8]. Currently, various nanomaterials, including silver nanoparticles [9], zinc oxide nanoparticles [10], and graphene oxide [11] have accelerated the wound healing to a certain degree, but most of them can only contribute to the individual healing stage, lacking comprehensive strategies for hierarchical stimulation and regulation of the wound healing process [12]. Therefore, it is imperative to construct a multifunctional nanoplatform capable of meeting the demands of different stages during wound healing.

Peer review under responsibility of KeAi Communications Co., Ltd.
* Corresponding author. Frontier Institute of Science and Technology, Xi'an Jiaotong University, Xi'an, 710054, China.
E-mail address: rayboo@xjtu.edu.cn (B. Lei).
[1] These authors contributed equally to this work.

https://doi.org/10.1016/j.bioactmat.2023.01.019
Received 29 August 2022; Received in revised form 24 January 2023; Accepted 26 January 2023

Bioactive glass nanoparticles (BGN) are a unique class of biomaterials that have demonstrated the great potential in the field of skin tissue regeneration as they are able to accelerate the re-epithelization [13], enhance the angiogenesis [14] and modulate the inflammatory responses [15]. Additionally, BGN has also been reported to be biodegradable during the tissue repair. The biodegradation of BGN is a multi-factorial and long-term process involving hydration, hydrolysis and ion exchange events, which ultimately lead to the Si–O–Si network disintegration, where the released bioactive ions may function constantly through the stimulation of cell behavior [16,17]. More and more studies have demonstrated that bioactive ions (*e.g.,* $Ca^{2+}$and SiO_4^{4-}) released from BG have the capability to regulate the fate of cells and their interaction by activating paracrine effects during the wound healing process, such as stimulating the interactions between human dermal fibroblasts and human umbilical vein endothelial cells, and subsequently promoting the vascularization and extracellular matrix protein deposition [18,19]. More interestingly, bioactive glass is a type of silicate-based biodegradable material that plays a dual role in hemostasis. The Ca ions released from bioactive glass act as the cofactors contributing to the orientate protein assemblies and enzymes participating in fibrin production and coagulation cascades and the high-surface area of bioactive glass is important for effectively supporting thrombosis [20]. However, as BGN has mechanical rigidity and brittleness that is closer to those of hard tissue, the primary requirement for BGN in contact with skin tissue is the ability to form the stable long-term interfacial bonding [21,22]. BGN surface modification has been employed as a means of improving the interactions between the BGN surface and tissue, in addition to enhancing their stability in a physiological environment. Our previous studies have demonstrated that the decorating with β-glycerol phosphate disodium or fetal bovine serum is beneficial in BGN applications *in vivo* [23,24]. On the other hand, the multi-module assembly based on the nanotechnology is expected to provide opportunities for designing and creating BGN combining different functional structures to satisfy the multiple needs during wound healing. However, there have been relatively few reports on BGN that is designed through bioactive molecular assembly strategies and directly provides sequential therapy (hemostasis, inflammation regulation and cell proliferation) in wounds.

In this study, we propose to construct a multifunctional bioactive nanoglass platform (BGN@PTE) that continuously adheres to the topographically irregular tissue surface, activates the coagulation cascades, efficiently controls the hemorrhaging, sequentially regulates the inflammation, and promotes the cellular proliferation and skin reconstruction. The key to this strategy is the adoption of poly-tannic acid (PTA) and cationic antibacterial polypeptide ε-polylysine (EPL) to functionalize the BGN through the layer-by-layer assembly to effectively control bleeding *via* multiple dependent approaches and simultaneously accelerate wound repair (Scheme 1). To afford the tissue adhesive capacity, mussel-inspired tannic acid (TA), which is a typical plant polyphenol, is introduced in BGN. TA can bind strongly with different surfaces through the formation of various chemical bonds (*e.g.,* Michael addition/Schiff-base reaction and polyphenol-metal coordination) and non-covalent interactions (*e.g.,* hydrogen bonding and electrostatic interactions) [25]. More specifically, the catechol structure in TA is easy to

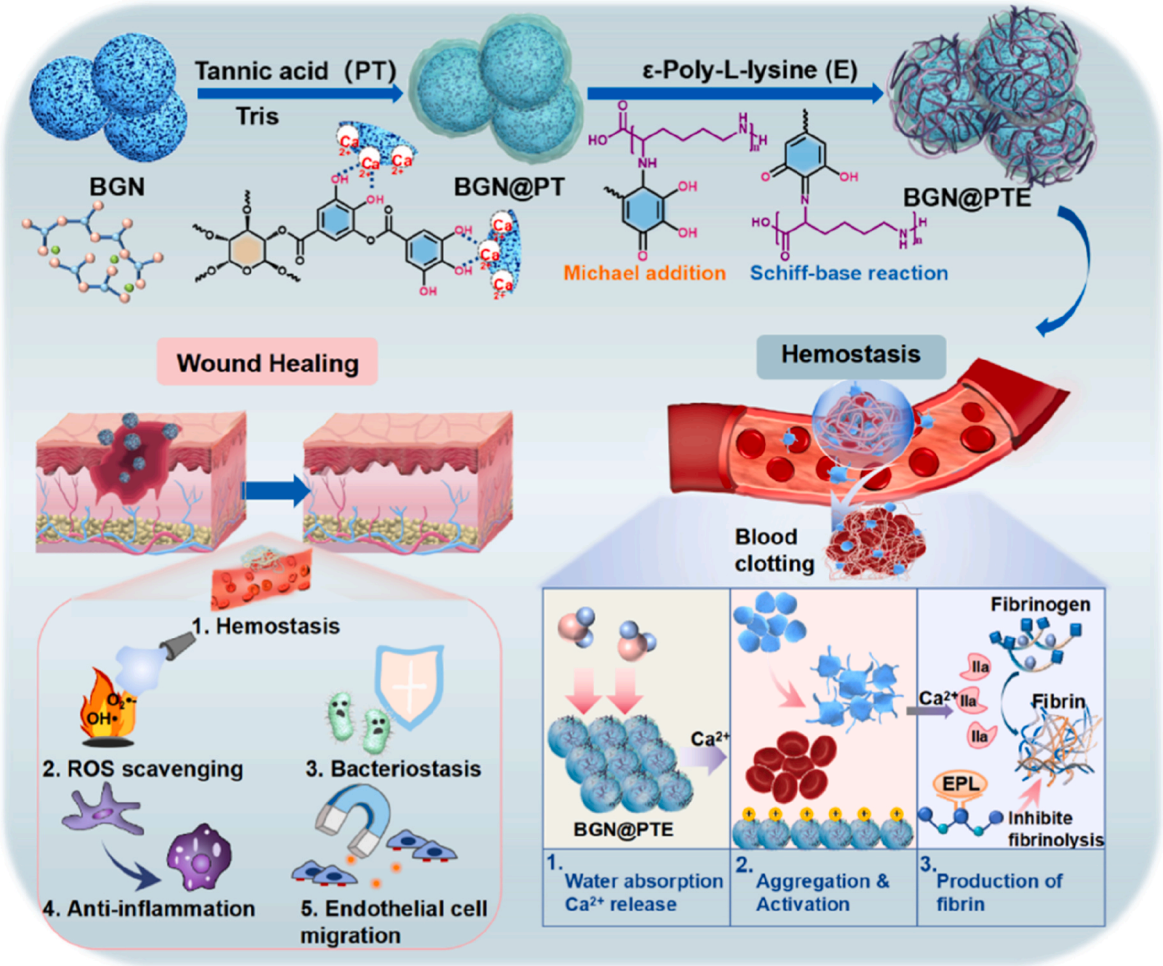

Scheme 1. Illustration of the synthetic route of the multilayer-structured BGN@PTA nanosystem. Based on the synergistic effect of a variety of components, BGN@PTE has excellent hemostasis functions and promotes multiple wound healing stages.

be oxidized into a quinone state under alkaline conditions, which subsequently could link with the amine groups through the Michael addition or Schiff base reaction, thus offering the opportunity to react with amine or thiol groups and forming stable covalent connections [26,27]. Notably, TA has also attracted significant attention in regenerative medicine due to its unique bioactivities such as anti-inflammatory and antioxidant activities as well as the hemostatic features [28,29]. Previous studies have also verified that TA-coated mesoporous silica can act as the molecule glue to adhere and astringe the wound, thus reducing blood loss [30,31]. As the nature of blood clot formation is gradual, the hemostatic agent must have a strong wet adhesion capability while also rapidly activating platelets and triggering the coagulation system. EPL is known as a natural antibacterial polypeptide with broad-spectrum antibacterial activity, while its cationic nature can trigger a series of hemostatic responses, augment the generation of thrombin, stabilize fibrin, and induce the aggregation of blood platelets [32]. In addition to examining the physicochemical properties of BGN@PTE, *in vitro* studies were conducted to explore the coagulation mechanism and biological activity. Furthermore, we investigated the hemostatic efficacy of this powder in a liver and tail vein hemorrhage model and the role in full-thickness skin defect repair.

2. Materials and methods

2.1. Preparation of BGN@PTE

The binary BGN with the composition of SiO_2–CaO (mol.%) = 80: 20, 60:40, 40: 60 was obtained by a sol-gel method, modified based on a previous study [33]. Dodecylamine (DDA) was used as a catalyst and template agent. Tetraethyl orthosilicate (TEOS) was used as the precursor for the hydrolysis and condensation in the presence of DDA to form Si–O–Si network. Different concentrations of the Ca^{2+} precursors could be added during the hydrolysis and condensation of TEOS. The details of the synthetic procedures are displayed in the supporting information. To prepare BGN@PT, 20 mg of BGN (Si_{60}–Ca_{40}) was dissolved in 40 mL of 10 mM Tris (hydroxymethyl) aminoethane (Tris)-HCl buffer (pH 8.5), followed by the addition of 80, 40, 20, 10 and 5 mg of tannic acid. The prepared BGN@PT was named as BGN@PT1, BGN@PT2, BGN@PT3, BGN@PT4 and BGN@PT5, respectively. The reaction mixture was strongly stirred at the room temperature for 24 h. After that, BGN@PT was separated by centrifugation and washing and then freeze-dried for subsequent use. Next, the obtained BGN@PT4 was covalently functionalized with EPL. In a pH 9.0 buffer solution, BGN@PT was mixed with EPL at a mass ratio of 1:2 and then stirred for 24 h. The prepared BGN@PTE was centrifuged and washed three times with deionized water to remove excess EPL.

2.2. Characterization

The surface morphology and composition of BGN were examined by a field emission scanning electron microscope (FESEM, Gemini SEM 500, Zeiss) equipped with an energy-dispersive spectrometer (EDS). The surface area and pore size of the prepared BGN was characterized by a volumetric adsorption analyzer (ASAP 2460, Micromeritics) based on the Brunauer-Emmett-Teller (BET) method. The morphologies of BGN, BGN@PT, and BGN@PTE were observed using a transmission electron microscopy (TEM, H-8000, Hitachi) at an accelerating voltage of 100 kV. The chemical structure of samples was tested using Fourier transform infrared spectroscopy (FTIR, TENSOR 27, Bruker) and X-ray photoelectron spectroscopy (XPS, ESCALAB Xi+, Thermo Fisher). The zeta potential was detected using a Malvern Mastersizer (Nano ZS, Malvern Instruments) at room temperature. Thermogravimetric analysis (TGA, STA 449C, Netsch) was performed to estimate the PTA and EPL content in BGN@PTE.

2.3. In vitro hemolysis assay and hemostatic evaluation

Kunming (KM) mice were purchased from the Laboratory Animal Center, Xi 'an Jiaotong University Health Science Center. The *in vivo* experiments were conducted according to the Animal Care and Use Committee (IACUC) of Xi'an Jiaotong University (2019-1167). Briefly, the fresh whole blood was drawn from Kunming mice, immediately collected in a tube with heparin sodium, and used for a series of *in vitro* hemolysis and hemostatic studies. The granular chitosan hemostatic agent (CELOX®) was used as a commercial control. The PBS-diluted blood was co-incubated with different materials, and the hemocompatibility was assessed using a spectrophotometer. The blood clotting index (BCI) assay was carried out according to the modified procedures as previously reported [34]. The quantitative platelet adhesion abilities of BGN, BGN@PT and BGN@PTE were evaluated by a photospectrometric measurement based on the determination of lactate dehydrogenase (LDH) activity [35]. The number of adherent platelets on the different sample surfaces was determined by measuring the LDH activity from the lysed solution of adherent platelets and comparing it with the corresponding calibration curve. The quantitative red blood cells (RBCs) adhesion performances of BGN, BGN@PT, and BGN@PTE were evaluated in the diluted whole blood using modified procedures. The experimental details were described in the supporting information. For the morphology characterization of platelets and RBCs on the hemostatic materials, 10 mg of samples (Celox, BGN, BGN@PT and BGN@PTE) were compressed into slices before the test and then were placed in a 24-well plate, respectively. Platelet-rich plasma (PRP) was obtained by centrifuging the whole blood at 2000 rpm for 10 min. Whole blood or PRP (100 μL) was dropped onto the samples surface and then placed at 37 °C for 30 min, respectively. Subsequently, all samples were washed with plenty of PBS to thoroughly wash the nonadherent platelets and erythrocytes away. To characterize the morphology of RBCs and platelets, a solution of glutaraldehyde (2.5%) was used to fix the samples for 4 h at 4 °C and gradually dehydrated by immersing them in 60%, 70%, 80%, 90%, and 100% ethanol solution step-by-step. After being dried, different samples were pre-coated with a gold layer and observed by SEM.

2.4. Cytocompatibility and cell migration analysis

To evaluate the cytocompatibility of BGN@PTE, mouse fibroblast (L929) cells, human umbilical vein endothelial cells (HUVECs) and mouse mononuclear macrophage leukemia (RAW 264.7) cells were seeded in 96-well plates at a density of 1×10^5 cells mL^{-1}. The cells were treated with as-prepared leaching solutions of BGN@PTE at different concentrations for 24 h. Subsequently, the cell viability was measured by Alamar Blue assay. The migration of HUVECs in the leaching solution of BGN@PTE was carried out according to a typical scratch assay [36]. The detailed process was available in the supporting information.

2.5. In vitro evaluation of cytokine expression

For the evaluation of cytokine expression, 100 ng mL^{-1} of lipopolysaccharide (LPS) was incubated with RAW264.7 cells for 16 h to obtain the inflammation-activated cells. The total RNA from RAW264.7 cells after BGN, BGN@PT and BGN@PT treatments was extracted using the TRIzol reagent. Similarly, the total RNA was isolated from all the groups of HUVECs. The expression levels of tumor necrosis factor-α (TNF-α), interleukin-1β (IL-1β), vascular endothelial growth factor (VEGF), and hypoxia-inducible factor-1α (HIF-1α) were measured by the real-time quantitative polymerase chain reaction (RT-qPCR). The detailed experimental procedure used in this assay was specifically described in the supporting information.

2.6. Extracellular and intracellular antioxidant properties

1,1-Diphenyl-2-picryl-hydrazyl (DPPH) was employed to evaluate the general free radical scavenging activity of BGN@PTE. The detailed process was described in the supporting information. 2,7-Dichloro-dihydrofluorescein diacetate (DCFH-DA) was chosen to assess the intracellular antioxidant capacity of BGN@PTE. RAW 264.7 cells (1×10^5) were seeded in slides and cultured overnight, and the cells were treated with LPS for 24 h to induce the cell polarization. After washing twice with PBS, the cells were incubated with a dispersion of BGN, BNG@PT and BGN@PTE for 8 h respectively. Subsequently, the cells were washed with PBS, cultured with DCFH-DA (10 μM) at 37 °C for 30 min and washed again before observation under a confocal laser scanning microscope. The fluorescence intensity was analyzed for three acquired images for the average intensity based on the mean gray value calculation of ImageJ software.

2.7. In vivo hemostasis study

A mouse-liver trauma model was employed to assess the *in vivo* hemostatic potential of the styptic powders (Celox, BGN, BGN@PT, BGN@PTE), where Celox was used as a commercial control. Briefly, female mice (6–7 weeks) were first anesthetized and fixed, and then the abdomen of the mice was operated on exposing the middle lobe of the liver. To calculate the bleeding volume, the pre-weighed filter paper was placed underneath the liver. The cut wound (length: 6 mm) was induced using a scalpel on the liver. 5 mg of powders was immediately applied to the bleeding position, respectively. The group without any treatment after liver bleeding served as a blank control group. The blood loss and hemostasis time were recorded during the whole hemostatic process. For H&E staining analysis, the liver tissues with the incision were first fixed in a 4% formaldehyde solution for 24 h. Following fixation, the samples were dehydrated using alcohol (70%, 80%, 95%, and 100%) and then immersed in xylene, and embedded in paraffin. Paraffin-embedded samples were cut into 5 μm sections, which were dewaxed using xylene and hydrated using the gradient alcohol. Then, the slides were stained with hematoxylin and eosin in turn. The sections were visualized on an optical microscope (Olympus BX53).

To evaluate the hemostatic potentials of BGN@PTE in the mouse tail-amputation model, female KM mice with a body weight of approximately 30 g were randomly divided into five groups. The mouse was fixed and the proximal tail vein was cut off 30% length of the tail, followed by leaving the tail in air for 5 s, and then treatment with Celox, BGN, BGN@PT, BGN@PTE and a group without any treatment as a negative control (n = 4). Hemostatic performance was assessed by investigating the blood loss for all groups within 90 s.

2.8. In vivo wound healing effect

Forty KM female mice (8-week-old, 30 g) were randomly and equivalently divided into five groups. The operation was performed under anesthesia. After shaving the hair off their backs, two full-thickness defect areas with a diameter of 8 mm were symmetrically created on the mouse back. 10 mg of powder (Dermlin™, BGN, BGN@PT, BG@PTE) was distributed evenly over the wound, whereas the control mice were treated with Tegaderm film (3 M). Dermlin™ is a commercial bioactive glass powder dressing and was used as a control in this study. In order to prevent the skin from shrinking, a 3 M film was pasted around the wound. For visualization, the wound healing process was monitored and recorded by photographing wounds from day 0 to day 14. The tissues in the wound bed were removed at corresponding time points and immersed in formaldehyde, and then subjected to histological analysis by using H&E staining. For the analysis of wound healing, the wound areas were measured by ImageJ software and the wound closure rate was calculated as the percentage of the initial wound area with a diameter of 8 mm. Hair follicles were counted on three different H&E samples per group at a magnification of 4 X. The width of immature tissue was measured on H&E samples by ImageJ software and averaged from three different samples per group. The epidermal thickness was measured using ImageJ on three different H&E samples per group at three positions along the epidermis. The blood vessels and the inflammatory response in each group were systematically evaluated by the immunofluorescence. The quantitative fluorescence intensity analysis was performed using ImageJ software on an average of three images. The average intensity inside a region of interest (ROI) around the wound was computed for each image at 20 X. The fluorescence intensity was normalized by the wound area of the selected area.

2.9. Statistical analysis

All data in this article were denoted as the mean ± standard deviation. All data were analyzed by an ordinary one-way analysis of variance (ANOVA). A value of $P < 0.05$ (*) was considered statistically different.

3. Results and discussion

3.1. Synthesis and characterization of the BGN@PTE nanoplatform

The release of Ca^{2+} from the amorphous network of BGN could participate in the clotting process by promoting the activation of the coagulation pathway [37]. Therefore, in this work, we synthesized the BGN with high CaO content. During the formation of the SiO_2 network, the active Si–OH and Si-containing oligomers can react with the Ca precursor to gradually form Ca-doped silica nanoparticles with a Si–O–Ca hybrid framework. TEM images exhibited that BGN with different CaO contents were all monodispersed nanospheres and had a rough surface (Figs. S1a, b, c). In addition, BGN showed a gradually increasing particle size and decreased specific surface area with increased Ca feeding content (Figs. S1g, h, i, j, k, l). The actual content of Ca in the prepared BGN could be tuned by adjusting the feeding ratios of TEOS and $Ca(NO_3)_2$ (Si: Ca = 80:20, 60:40, 40:60). The maximum calcium content can be reached for BGN by adjusting the feeding Si: Ca ratio was 60:40. The corresponding EDS results showed that atomic ratios of Si, Ca, and O in the obtained BGN (60Si40Ca) were 24.42%, 10.45%, and 65.12%, respectively (Fig. S1e). However, there was a reduced content of calcium incorporation into the glass network when the Si: Ca ratio further was decreased (Si: Ca = 40:60). Therefore, the ratio of Si: Ca = 60:40 was found to be optimal from the calcium content perspective, and the BGN (60Si40Ca) was used for the subsequent modification.

The as-prepared BGN showed a spherical morphology with a uniform particle size of approximately 202.9 nm (Fig. 1a). Subsequently, BGN@PT was fabricated based on the coordination interactions between Ca ions and TA and further self-polymerization of TA in a weak base environment. The TEM images in Fig. 1a clearly reveal the core-shell structure of BGN@PT, indicating that the PTA wrapping process on BGN was successful. EPL was grafted onto the surface of BGN@PT through a Michael addition/Schiff-base reaction between the amine group of EPL and PTA, where the morphology differences between BGN@PT and BGN@PTE were less pronounced. The observation of BGN@PTE at a higher magnification revealed that approximately a 5–10 nm thick layer consisting of PTA and EPL was wrapped on the surface of BGN (Fig. S2).

FTIR spectra further recorded the layer-by-layer assembled structure of BGN@PTE (Fig. 1b), where the BNG@PTE spectra exhibited an intense and broad absorption peak at 1080 cm^{-1} that can be assigned to the Si–O–Si asymmetric stretching vibrations, revealing the existence of a silica network from BGN. After being coated with PTA, the characteristic absorption peaks were observed at 1700, 1590 and 1500 cm^{-1}, corresponding to the C═O stretching vibration and the aromatic ring stretching vibration in PTA [38,39]. Several absorption peaks of BGN@PTE occurred at 2930 and 2860 cm^{-1}, which could be ascribed to

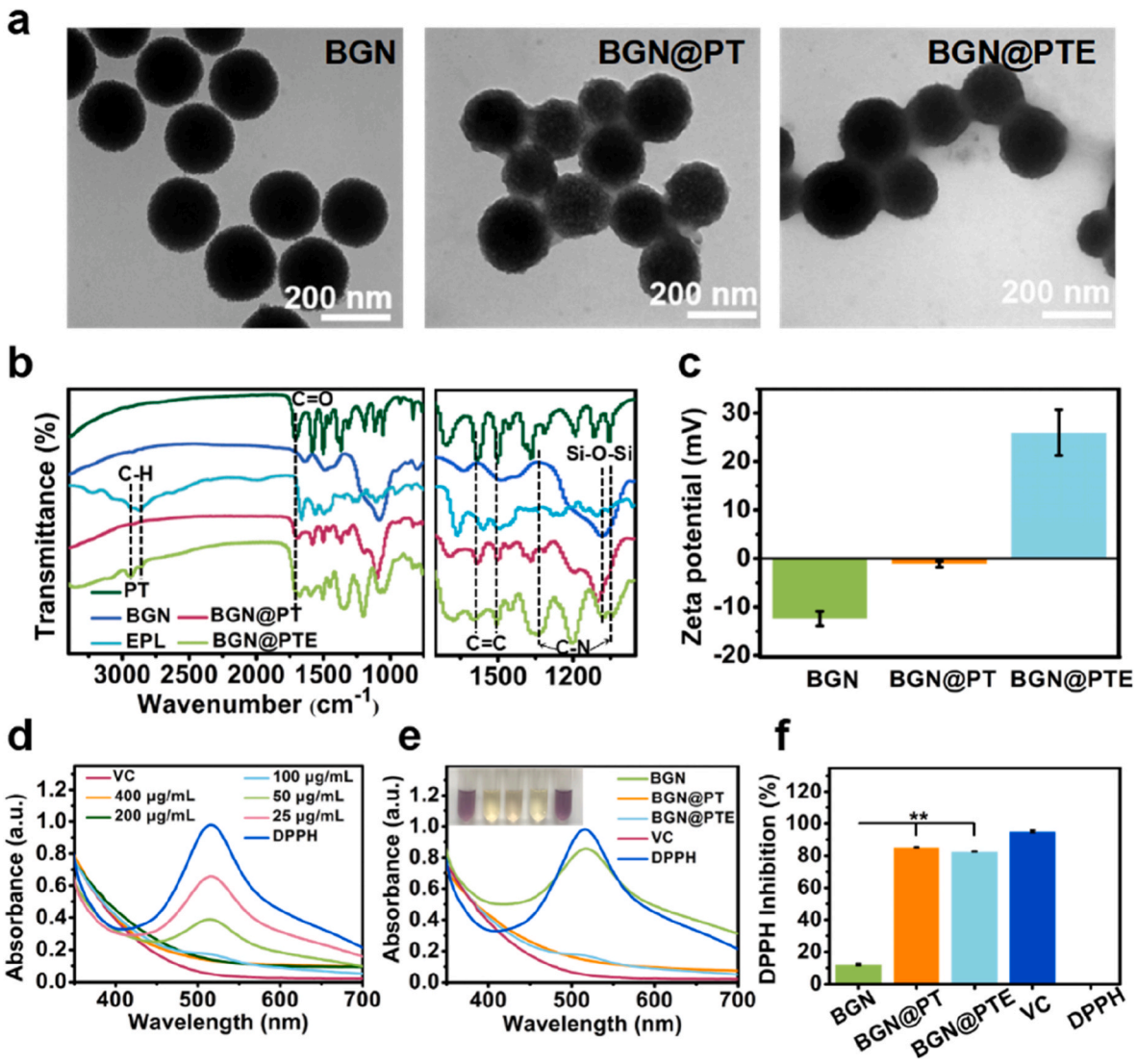

Fig. 1. Synthesis and characterization of BGN@PTE hemostatic agent. (a) TEM images of BGN (I), BGN@PT (II), and BGN@PTE (III). (b) FTIR spectra of PTA, BGN, EPL, BGN@PT, and BGN@PTE. (c) Zeta potentials of different nanoparticles in the formation of BGN@PTE. (d) UV–vis spectra of DPPH inhibition triggered by different concentrations of BGN@PTE for 30 min (VC: vitamin C). (e) UV–vis spectra and photographs (inset) of DPPH after culture with different materials for 30 min. (f) Comparisons of the relative free radical scavenging activity of different materials.

the C–H asymmetric stretching in EPL. Moreover, the presence of the new peaks at 1335 cm^{-1} and 1045 cm^{-1} were assigned to the aromatic C–N stretching vibration, which demonstrated the Michael addition reaction between the quinone groups of PTA and the amine groups of EPL [40]. Furthermore, X-ray photoelectron spectroscopy (XPS) was also conducted to investigate the reaction between PTA and EPL (Fig. S3a). When focusing on the N 1s spectra of the BGN@PTE, the spectrum can be resolved into three peaks at 399.4, 400.2, and 401.8 eV, which were attributed to C–N, C═N, and C–NH_3^+, respectively [41,42]. The presence of the C═N bond verified the formation of a Schiff base bond between PTA and EPL. Collectively, it can be conjectured that the quinone groups in PTA coating could function as the active sites to cross-link with the amine groups of EPL through a Schiff base/Michael addition reaction. Additionally, changes in the zeta potential during the preparation of BGN@PTE verified the successful layer-by-layer modification on BGN. Initially, the bare BGN cores exhibited a negative zeta potential (−12.37 mV) in PBS buffer solution (pH = 7.4), which may be due to the presence of Si–OH bonds on their surface (Fig. 1c). After coating with the PTA layer, the zeta potential of BGN@PT increased to −1.15 mV, whereas BGN@PTE had a positive value of 25.97 mV, which may be attributed to the amine groups from EPL. Overall, all results confirmed that PTA and EPL had been anchored on the surface of the BGN.

Thermogravimetric analysis (TGA) was performed to confirm the coating formation and to estimate the PTA and EPL content in BGN@PTE (Fig. S3b). The TGA curve of BGN, BGN@PT and BGN@PTE showed the major weight loss over the temperature range from 25 to 800 °C. Compared with BGN, BGN@PT showed an additional weight loss of 14.71%, which was due to the thermal degradation of PTA coating. Compared with BGN@PT, BGN@PTE showed an additional weight loss of 10.72%. From the TGA curve, the content of the PTA and EPL in BGN@PTE was calculated to be about 12.98 wt% and 13.19 wt%, respectively.

The as-prepared BGN@PTE could degrade slowly as revealed by TEM images at different time points (Fig. S4), where the polymer degradation involved the layer morphology collapse and detachment from the BGN surface. Notably, the polymer surrounding the BGN was not completely degraded by day 14. Inductive coupled plasma mass spectrometry (ICP-MS) was used to determine the concentrations of Si and Ca in the obtained extracts, as shown in Table S1. After incubation for 48 h, it could be seen that the cumulative release of Si and Ca ions of BGN@PTE reached 79.5 mg/L and 115.5 mg/L, respectively. Notably, the Si

concentration in BGN extracts was slightly higher than that of group BGN@PT and BGN@PTE, which was probably attributed to the barrier effect of PTA and EPL layers that slowed down the ions release. To verify the PTA and EPL release from BGN@PTE after its exposure to the physiological environment, the PTA and EPL release was analyzed by high performance liquid chromatography (HPLC) and micro amino acid (AA) content assay kit, respectively. Based on the absorbance measurement, the concentration of EPL in the BGN@PTE extract can be calculated by using the calibration curve (Fig. S5a). The results showed that the concentration of EPL in the extracts for 2 days and 7 days was 670.06 and 2403.39 μg/mL, respectively. The release amount of EPL reached 18.22% on day 7, demonstrating that BGN@PTE was able to sustain the release of EPL over time. Besides, the PTA concentration from the BGN@PTE extract was determined by HPLC and monitored by UV absorbance detection at 254 nm (Fig. S5b). Semi-quantitative analysis of the peak area integration for the PTA at 3.9 min showed the appearance of PTA, where the PTA peak area corresponding to 7 days was approximately 4.4-fold that of 2 days. Overall, the bioactive ions and polymer layers had no burst release effect, allowing the sustained dose release in space and time and playing the role in the whole wound healing process.

3.2. In vitro antioxidant analysis

The 2,2-diphenyl-1-picrylhydrazyl (DPPH·) is a purple stable free radical compound with a characteristic UV–vis absorption peak at 517 nm, which can be reduced by antioxidant substances and thus has an indicative function in radical scavenging potential. Firstly, the influence of the concentration of BGN@PTE on their antioxidant activity was explored. The results displayed a concentration-dependent free radical scavenging behavior and DPPH· was rapidly scavenged within 30 min at 100 μg/mL of BGN@PTE (Fig. 1d). In addition, the DPPH· scavenging activities of different samples were determined by comparing the absorbance value at 517 nm, respectively (Fig. 1e). The results of the assay showed that the characteristic absorption of DPPH· was decreased significantly in the presence of BGN@PT and BGN@PTE, demonstrating their excellent free radical scavenging performances. Additionally, the digital photo was consistent with the absorbance change of the DPPH· solution, which exhibited nearly complete fading in the presence of BGN@PT and BGN@PTE, while the DPPH· solution treated with BGN showed no significant change. Thus, the results verified that the assembly of the PTA layer endowed BGN with remarkable free radical scavenging activity, which relied on the classical antioxidant mechanism of the transfer of a hydrogen atom from a phenolic group [43]. Moreover, the radical scavenging rate reached more than 80% for BGN@PT and BGN@PTE (Fig. 1f), whereas the slightly decreased radical scavenging rate of BGN@PTE may be due to the lower relative content of PTA in BGN@PTE than that of BGN@PT. Overall the prepared hemostatic agent showed excellent antioxidant activity and was promising for alleviating excessive oxidative stress in acute wounds.

3.3. Hemolysis and in vitro hemostasis evaluation

Furthermore, the hemocompatibility of BGN, BGN@PT and BGN@PTE was evaluated with fresh anticoagulant blood, where Triton X-100 served as the positive control. Notably, different from the bright red in Triton X-100 and BGN, the PBS, Celox, BGN@PT and BGN@PTE treatment groups had no obvious blood color shown in the photograph (Fig. 2a). The results of the calculation revealed that the hemolysis ratios of the BGN@PTE with different concentrations were all lower than 3%,

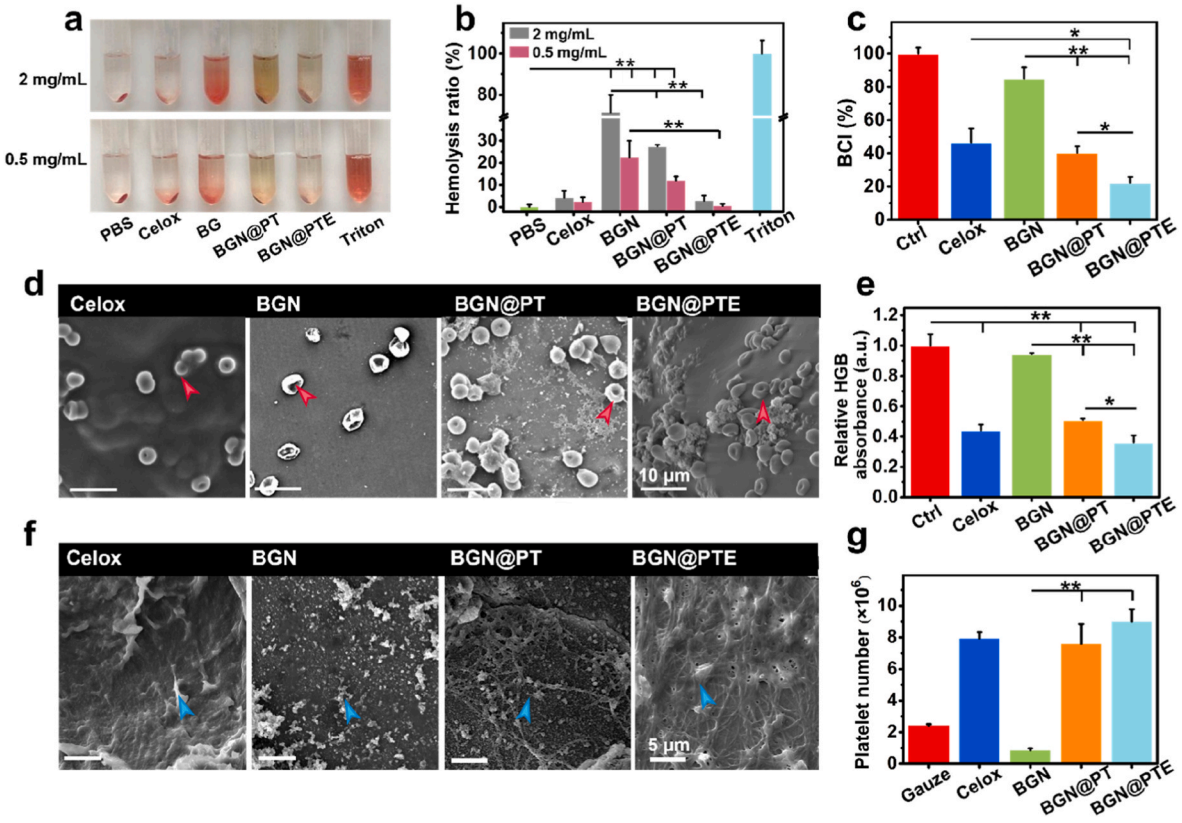

Fig. 2. Hemocompatibility and *in vitro* blood clotting performance of BGN@PTE. (a) Whole blood treated with PBS, Celox, BGN, BGN@PT, BGN@PTE and Triton. (b) Hemolysis ratios of samples (n = 3). (c) BCI of different materials (n = 3, $*p < 0.05$, $**p < 0.01$). (d) SEM images of RBCs (red arrow) adhesion and aggregation on the surface of Celox, BGN, BGN@PT and BGN@PTE. (e) HGB content of adherent RBCs in different hemostatic materials after incubation with diluted whole blood (n = 3, $*p < 0.05$). (f) SEM images of platelets (blue arrow) adhesion and activation on the surface of Celox, BGN, BGN@PT and BGN@PTE. (g) The number of adhered platelets after being treated with different hemostatic materials (n = 3, $*p < 0.05$).

whereas the BGN exhibited a certain extent of hemolysis, which was far higher than the safety scope (5%) (Fig. 2b). Hence, it was considered that the good blood compatibility of BGN@PTE could be ascribed to the PTA and EPL modification. The morphology observation revealed that the RBCs treated with BGN@PTE had a complete shape and a smooth surface (Fig. S6). In short, BGN@PTE exhibited excellent hemocompatibility and could be a safe hemostatic dressing for further *in vivo* applications.

The effect of the different PTA coating amounts in BGN on blood clotting *in vitro* was assessed *via* the measurement of BCI. As a quantitative index for the evaluation of the blood coagulation performance of various materials, the higher the BCI value, the slower the coagulation rate. In this experiment (Fig. 2c), compared with BGN (BCI = 85.1%), BGN@PT had the lower BCI value (40.2%), indicating that PTA surface modification showed superior hemostatic performance. More interestingly, with the decrease in the mass ratio between TA and BGN, BGN@PT4 reached a threshold of optimal hemostasis (Fig. S7). Therefore, the subsequent surface modification was made on the basis of BGN@PT4. We believe that under such a mass ratio, the nanoscale morphology of BGN, PTA coating thickness, and Ca^{2+} ions released from BGN would contribute to achieving a satisfactory multipath synergistic hemostatic effect. On this basis, EPL was then grafted onto the BGN@PT4 surface as expected to lead to the additional blood coagulation performance improvements *via* triggering the clotting cascade. Furthermore, the clotting ability of different materials was quantified by calculating BCI. The BCI of the BGN@PTE groups was about 22%, which was lower than that of the BGN@PT group by approximately 18%, suggesting that the introduction of EPL significantly increased the blood clotting rate. Meanwhile, it is worth noting that BGN@PTE was superior to the current commercial Celox (46%) from the perspective of BCI.

In view of the importance of the adhesion of RBCs and platelets to hemostatic performance, the influence of BGN@PTE on the cell adhesion behavior was observed by SEM to explore their underlying hemostatic mechanism. As shown in Fig. 2d, there were numerous RBCs were adhered and aggregated on the BGN@PTE surface, which showed powerful blood cell binding ability. Additionally, SEM images revealed the morphology of RBCs, a complete surface and aggregated distribution of RBCs with round cake shapes in the BGN@PT and BGN@PTE groups, while the RBCs in BGN did not exhibit good morphology. Simultaneously, the absorbance of free hemoglobin (HGB) after incubation was measured to quantitatively analyze the number of free RBCs, where the lower absorbance values indicated that more RBCs adhered to the surface of the materials (Fig. 2e). BGN@PTE exhibited a similar ability to adhere to erythrocytes as Celox, while its relative hemoglobin absorbance was significantly lower than that of the BGN and BGN@PT groups, which was consistent with the observation from SEM, demonstrating the superior hemostatic potential of BGN@PTE.

When in contact with blood, the effective hemostatic materials generally stimulate the platelet adhesion and aggregation, which further leads to the activation of clotting events. To reveal this point, the interaction of platelet-rich plasma with different materials was observed by SEM. As shown in Fig. 2f, only a few platelets adhered to BGN, which was less than that in the BGN@PT and BGN@PTE groups. Not only that, it was found the adherent platelets in BGN@PT deformed and extended many pseudopods, and fibrin aggregates were closely connected to the materials, which suggested that BGN@PT significantly induced platelet activation and fibrin production. Moreover, the cationic groups of EPL might further exert hemostatic capability by electrostatic force-mediated platelets bridging. As confirmed by SEM images (Fig. S8), there was a denser fibrin mesh formed with platelets trapped in it *via* the interaction between the BGN@PTE and platelets, which indicated that the presence of EPL allowed internal aggregation and activation of platelets, in favor of the process of hemostasis. By comparison, although Celox was also able to induce platelet activation, the overlapping fibrous network structures were not observed. Then, the quantitative platelet adhesion was determined by the lactate dehydrogenase (LDH) method (Fig. S9), where the platelet numbers were converted from the absorbance of LDH as displayed in Fig. 2g. After the 60 min incubation, the number of platelets adhered to the BGN@PTE was remarkably higher compared with gauze and BGN, whereas there was no significant difference compared with Celox and BGN@PT. Therefore, the excellent hemostasis capability of BGN@PTE was contributed to the multiple proposed mechanisms. On the one hand, the high specific surface area and large porous structure of BGN ensure the rapid absorption of blood and contribute to concentrating of blood clotting factors activated by Ca^{2+} [44]. On the other hand, the PTA layer of BGN@PT renders it superior in trapping erythrocytes, promoting platelet aggregation and triggering platelet activation simultaneously. More interestingly, we found that the introduction of EPL contributed to the formation of a denser fibrin network, which may be attributed to the EPL enhancing thrombin and fibrin production as well as retarding fibrinolysis, which is critical for the formation of blood clots [32].

3.4. Cytocompatibility and cell migration evaluation of BGN@PTE in vitro

RAW 264.7 cells, L929 cells and HUVECs were co-cultured with the leach solution of BGN@PTE respectively to verify the cytocompatibility. Under different concentrations of the BGN@PTE leach solution, the leach solution could not adversely affect the viability of either L929 cells or HUVECs even at the highest concentration of 8 mg/mL, and could promote the proliferation of RAW 264.7 cells after a 24 h treatment (Fig. 3a, b, c). It is acknowledged the migration and recruitment of HUVECs is a crucial process in angiogenesis. Afterward, we examined the effects of BGN@PTE on HUVECs migration by a scratch assay. After treatment for 36 h, the extent of cell migration in the BGN@PTE group was significantly different from the control group, as observed by the changed closure of the scratch area (Fig. 3d). Meanwhile, the quantitative analysis result was consistent with the observation. At all the time points (12 h, 24 h, 36 h), BGN@PTE was able to induce HUVECs to migrate at a significantly faster rate in scratch, whereas the cells in the control group exhibited a slow migration. More specifically, the relative scratch width of the BGN@PTE group was almost completely closed at 36 h, but the relative healing rate of the control group was only 31.5% (Fig. 3e), suggesting that the mobility of HUVECs was significantly enhanced under BGN@PTE treatment. Accelerated angiogenesis is crucial in wound healing and depends on the participation of various growth factors, such as VEGF. Thus, the expression of VEGF in HUVECs was determined by RT-qPCR assay at the gene level (Fig. S10). It could be observed that all the extracts of BGN, BGN@PT and BGN@PTE up-regulated the gene expression of VEGF in HUVECs (Fig. S10a), indicating that the released bioactive ions may play a positive role in angiogenesis *in vitro*. Interestingly, the expression of VEGF genes in BGN@PTE was significantly higher than that in BGN and BGN@PT groups. To further explore the mechanism of BGN@PTE extracts affecting VEGF expression, the effect of the extracts on the upstream factor HIF-1α was evaluated (Fig. S10b). The gene expression level of HIF-1α in HUVECs was significantly up-regulated with the stimulation of BGN@PTE extracts compared with other groups, which confirmed that the released EPL from BGN@PTE promoted the expression of the HIF-1α gene, thus achieving the purpose of pro-angiogenesis by the synergetic effect of the bioactive ions and EPL.

3.5. Antiinflammation and intracellular ROS scavenging evaluation

During the immune response, LPS stimulates immune cells to secrete various inflammation-related cytokines [45]. It is a major strategy to regulate the complex inflammatory environment for wound repair. Herein, LPS-induced RAW264.7 cells were used to explore the anti-inflammatory effects of BGN@PTE. The expression of representative genes, such as TNF-α and IL-1β was chosen as indexes to investigate the anti-inflammatory efficacy (Fig. 3f and g). The results showed that

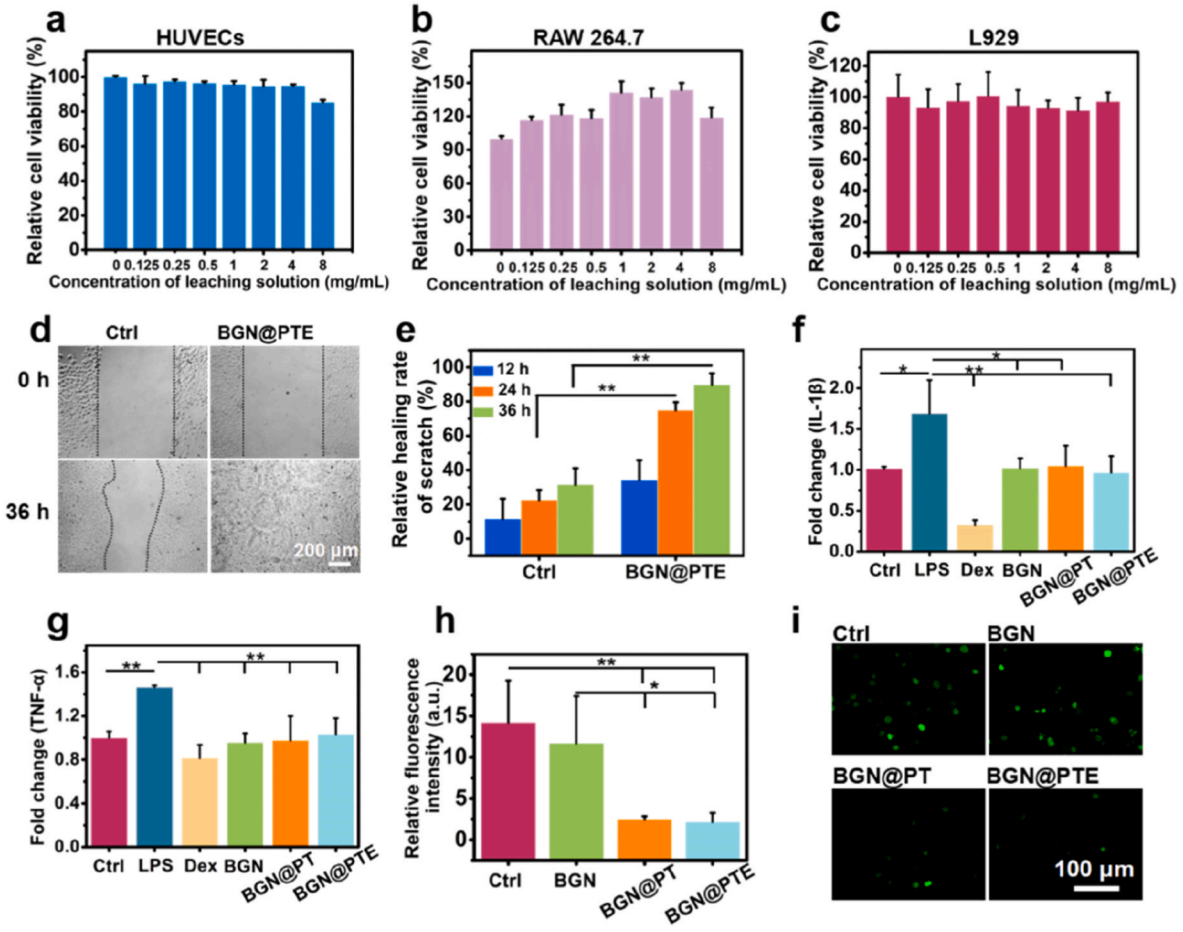

Fig. 3. Cytocompatibility, cell migration and anti-inflammatory effect of BGN@PTE. Relative cell viability for HUVECs (a), RAW 264.7 cells (b), L929 cells (c) after incubation with the leaching solution of BGN@PTE (n = 5). (d) Representative optical images of scratches and the migration ratio of HUVECs (e) when co-cultured with leaching solutions of BGN@PTE (n = 3, $*p < 0.05$, $**p < 0.01$, Scale bar: 200 μm). The cells without the leaching solutions were set as a control. The mRNA expression of the pro-inflammatory cytokines IL-1β (f) and TNF-α (g) in RAW264.7 cells (n = 3, $*p < 0.05$, $**p < 0.01$). (h) Quantitative statistics of the CDF fluorescence signal. (i) CLSM images of LPS-induced RAW 264.7 cells stained with DCFH-DA after various treatments for intracellular ROS detection (scale bar: 100 μm).

the mRNA expression of TNF-α and IL-1β in cells was markedly up-regulated after LPS treatment. In contrast, the leach solutions of BGN, BGN@PT and BGN@PTE were able to significantly suppress the production of pro-inflammatory cytokine TNF-α in LPS-induced RAW264.7 cells. Besides, BGN, BGN@PT and BGN@PT also presented a potent anti-inflammatory activity *via* regulating the expression of IL-1β. The results confirmed that a persistent inflammatory state was relieved by BGN@PTE, which was promising for promoting the wound transit to the regeneration stage smoothly.

The excessive ROS mediated by the disordered immune response around wound tissues could cause oxidative damage and extracellular matrix (ECM) destruction, resulting in delayed wound healing. Therefore, we further assessed the potential effect of BGN@PTE on scavenging intracellular ROS (Fig. 3 h, i). It could be found LPS treatment stimulated the ROS production in RAW264.7 cells, whereas BGN@PT and BGN@PTE seemed to relieve the intracellular oxidation after incubation for 8 h, as displayed by the significantly decreased green fluorescence. Collectively, these results indicated that BGN@PTE could effectively reduce the intracellular ROS level, which was contributed to the excellent antioxidant capacity of PTA, thus facilitating wound healing.

3.6. Antibacterial activity evaluation

Conventional powder wound dressings cannot form a protective barrier, making it difficult to prevent wound beds from bacterial infection, which often seriously retard wound healing. The outstanding antibacterial capacity of PTA and EPL inspired us to explore the antibacterial activity of BGN@PTE. Consequently, the antibacterial capacity of BGN@PTE was quantitatively investigated against gram-positive bacteria (*Staphyloccocus aureus*, *S. aureus*; and methicillin-resistant *Staphylococcus aureus*, MRSA) and gram-negative bacteria (*Escherichia coli, E. coli*). As shown in Figs. S11a, b, a great number of colonies appeared on the agar plates of the control group, while both BGN@PT and BGN@PTE inhibited the growth of *E. coli*, *S. aureus*, and MRSA. It is worth noting that BGN failed to produce any antibacterial effect on them, thus proving that the excellent antibacterial activities of BGN@PTE are derived from PTA and EPL. The quantitative statistical results (Fig. S11b) showed that the antibacterial effect of BGN@PT against *S. aureus* and MRSA was superior to that against *E. coli*, which may be attributed to the mechanism by which tannic acid could directly bind to the peptidoglycan layer in the membrane of gram-positive bacteria [46]. Additionally, BGN@PTE showed a higher antibacterial rate than BGN@PT because EPL has broad-spectrum antibacterial activity and destroys the bacterial membrane *via* electrostatic force. The synergetic effect of both PTA and EPL provides BGN@PTE with an excellent antibacterial effect, which is important for promoting wound healing.

3.7. Evaluation of hemostasis and tissue adhesion in vivo

The hemorrhages model of the liver in mice was used to evaluate the wound closure and hemostatic potential *in vivo* of BGN@PTE. The commercial hemostatic Celox was chosen as a control (Fig. 4a). Compared to the blank control without any treatment, the BGN group presented a slight reduction in blood loss (Fig. 4b). As we have observed, BGN could rapidly absorb blood in the initial hemorrhage but could not form a stable physical barrier. Although BGN@PT could initially seal the wound by inducing the aggregation of blood cells and platelets, a small amount of blood was still flowing out as the bleeding increased. The blood loss of the BGN@PT group was 29.9 mg, which was only approximately 15% of that in the blank control group (197.9 mg) and 36.9% of that in the BGN group (80.9 mg) (Fig. 4c). Remarkably, when applied to the wound, the BGN@PTE powder could firmly adhere to the wound sites with blood exudation, reducing the blood loss to 11.1 mg and exhibiting a hemostatic effect similar to Celox. The hemostasis time was also recorded (Fig. S12). The control group completely arrested bleeding for 106 ± 12.7 s, while the bleeding of the BGN group continued until 71 ± 14.3 s. In contrast, the time required to halt bleeding was much shorter with BGN@PT (27 ± 7.9 s) and BGN@PTE (18 ± 4.8 s). The significant reduction in both blood loss and hemostasis time suggested that BGN@PTE could efficiently achieve hemorrhage control in the liver incision model. These results showed that the introduction of PTA and EPL into the BGN surface can significantly enhance the *in vivo* hemostasis capability. From further analysis of the liver histological sections (Fig. 4d), it was observed that a large number of free RBCs were dispersed around the incision site in the control group, indicating that the wound was in a state of continued bleeding. In contrast, BGN@PTE may rapidly exert synergistic effects to control bleeding by aggregating RBCs and platelets forming blood clots at the incision surface. In addition, the formation of blood clots could seal the wound and prevent further bleeding from the internal tissue.

Next, the hemostatic performance of BGN@PTE was examined by using the mouse tail amputation model. It could be observed from Fig. 4e and f for the cutting tail in mice, there was continuous bleeding in

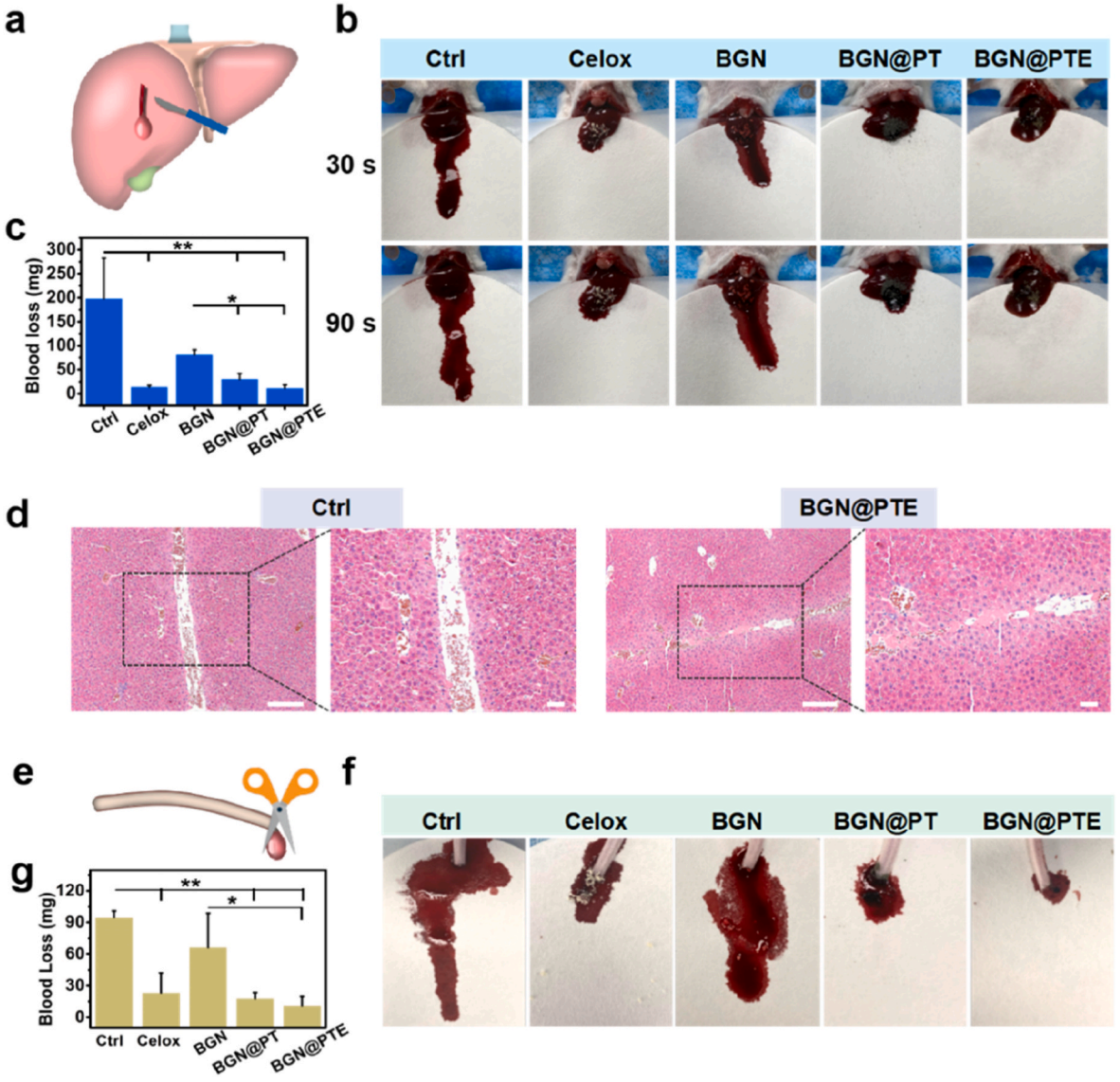

Fig. 4. Hemostatic capacity evaluation of BGN@PTE *in vivo*. (a) Schematic illustrations for inducing bleeding on mouse liver and stopping bleeding. (b) Photographs of livers and amount of bleeding after applying different hemostatic materials. (c) Quantitative statistics of lost blood from the bleeding liver. (H&E staining of the injured liver (control and BGN@PTE treatment, scale bar: 100 μm). (e) Schematic illustration of the tail vein bleeding model (n = 5, $*p < 0.05$, $**p < 0.01$). (f) Photographs of the amount of bleeding after tail amputation in different hemostatic material groups. (g) Quantitative statistics of lost blood from the injured tail vein (n = 4, $*p < 0.05$, $**p < 0.01$).

the blank control group, which showed that the highest amount of blood loss was 94.6 mg (Fig. 4g). However, after applying different hemostatic agents, the amount of blood loss in all four groups decreased to a certain extent. More importantly, only 10.7 mg of blood loss was measured when BGN@PTE was applied to the wound of the mouse tail vein, which was significantly lower than BGN with a blood loss of 66.5 mg. In summary, the significant reduction of blood loss in both the liver bleeding model and the tail amputation model suggested that the BGN@PTE possessed excellent hemostatic performance *in vivo* and applicability in complex bleeding sites.

Moreover, a linear full-thickness skin incision model (incision 2 cm) in rats was applied to further explore the adhesive performance of the BGN@PTE *in vivo*. Notably, the incisions failed to close in the control and BGN treatment groups, while the incisions treated with BGN@PT and BGN@PTE were well-closed and didn't tear as the rat moved (Fig. S13). The results indicated that the abundant quinone or catechol groups of the PTA layer provided the feasibility to construct adhesive interfaces so that the BGN@PT and BGN@PTE have firm adhesion to skin incision. The advantage in adhesion performance further proved that BGN@PT and BGN@PTE are promising for wound closure and healing as wound sealants.

3.8. Evaluation of wound healing in vivo

To validate the efficacy *in vivo*, BGN@PTE was further used as a wound dressing to repair full-thickness skin wounds. The wound sites (8 mm diameter) were covered with Dermlin powder (commercial inorganic dressing), BGN, BGN@PT and BGN@PTE, respectively. Representative pictures of the wounds in each group at scheduled time intervals are displayed in Fig. 5a. Macroscopically, it was observed that BGN@PT and BGN@PTE significantly accelerated the wound closure compared to 3 M as early as day 3. It was worth noting that the yellow pus scab was formed in the wound bed in the Dermlin and BGN groups on day 3, indicating that wound infection was almost inevitable in the external environment because powder dressings have the difficulty in blocking the environmental microorganisms from invading wounds. In contrast, the pus scab was hardly observed in the BGN@PT and BGN@PTE groups due to the effective bacteriostatic action of PTA and EPL. Until day 7, the BGN and Dermlin groups still displayed large defects in the wounds, and the wound healing rates of the BGN (74.6%) and Dermlin (76.4%) groups were far behind those of the BGN@PT (88.9%) and BGN@PTE (88.6%) groups (Fig. 5b). These results demonstrated that the uncontrollable infection would seriously hamper the healing process, whereas BGN@PT and BGN@PTE seemed to accelerate the wound healing through a multi-factorial coordinated action of inflammatory regulation, antibacterial activity, and scavenging of ROS. Additionally, BGN-treated wounds were healed similarly to the Dermlin-treated wounds (Fig. 5b and c), which was slightly better than that of the 3 M group and might be attributed to the release of bioactive ions. The BGN@PT and BGN@PTE treated groups showed the higher wound healing rates of 96.3% and 97.1% on day 14, respectively. The results indicated that the advantages of the layer-by-layer assembly of BGN@PTE could improve the wound healing from different phases.

Next, the tissues around the wound sites were further stained with hematoxylin-eosin (H&E) to investigate the impact of different treatments on the wound healing processes (Fig. 5d). On day 7, the histological analysis revealed that the wounds treated with BGN@PT and BGN@PTE achieved re-epithelialization in the center of the wounds. The control groups (BGN and Dermlin) showed a smaller amount of newly formed tissue, more local hemorrhagic focus, and looser connective tissue than the BGN@PT and BGN@PTE groups, thus demonstrating the benefit of the assembly layer of PTA for wound healing. With the prolongation of healing time, most wounds had complete epidermal covering with the exception of 3 M on day 14, in which the width of immature tissue in the BGN@PT and BGN@PTE groups was obviously narrower than that in the other groups (Fig. 5f). Subsequently, by counting the number of hair follicles (Fig. 5e), it was found that wounds treated with BGN@PTE developed abundant hair follicles with adjoining sebaceous glands within the wound bed on day 14. Additionally, BGN@PT and BGN@PTE treated wound tissues exhibited highly organized fibers as well as thinner and more uniform epidermis thickness, indicating accelerated recovery and satisfactory healing status (Fig. 5g). Taken together, these results demonstrated that BGN@PTE had an outstanding performance in promoting wound healing in full-thickness skin wounds.

To further reveal the role of BGN@PTE in wound inflammation, we assessed the proinflammatory cytokine expression of interleukin-6 (IL-6) in tissues harvested on day 3. As shown in Fig. 6a, c, the 3 M, Dermlin and BGN-treated wounds exhibited strongly positive IL-6 signals, indicating that the serious inflammation was still not controlled. In comparison, a distinct reduction of IL-6 expression in BNG@PT and BGN@PTE treated wounds could be found, which suggested that they could help to relieve inflammation. The anti-inflammatory properties of BNG@PT and BGN@PTE could be mediated by ROS scavenging and suppressing inflammatory cytokine expression. Neovascularization is a reliable indicator to reflect the efficacy of wound healing, in which the platelet endothelial cell adhesion molecule-1 (CD31), as a marker of vascular endothelial cells plays a vital role. Thus, the immunofluorescence staining of CD31 was conducted at the middle stage (day 7) of wound healing to evaluate the angiogenesis (Fig. 6b). The CD31 positive signals in wound areas treated with BGN@PT and BGN@PTE were significantly higher than in the control group. Quantitative analysis showed that the area of microvessels of the BGN@PT and BGN@PTE groups on day 7 was 1.78 times and 1.68 times of the control group (Fig. 6d), which evidently indicated that BGN@PT and BGN@PTE could promote vascularization. Altogether, these results suggested that BGN@PTE could greatly improve wound healing by regulating inflammation and reestablishing the blood vessel network *in vivo*.

Considering that the skin tissue response to injury occurs in an overlapping cascade but at a distinct stage, we constructed a versatile and programmable bioactive glass nanosystem for multi-stage control of wound healing and further explored the influence of BGN@PTE on the wound healing process. More excellent performance could be imparted to BGN by coating multilayer TA and antibacterial peptides on BGN through a layer-by-layer assembly. At the hemostatic stage, the BGN@PTE allowed rapid triggering of clotting as well as superior adhesive properties after the optimization of Ca^{2+} content and PTA coating thickness, while the grafting of EPL could further synergistically promote the blood coagulation by activating coagulation factor and increasing fibrin generation. In addition, previous studies have verified that platelet drives blood clot contraction by generating stress during clot maturation, which is thought to promote wound closure [47,48]. The BGN@PTE could also augment the conversion of fibrinogen to fibrin mesh, followed by driving blood clot formation, thus exhibiting the potential to promote wound healing, while the specific effect of hemostasis on wound repair is worthy of further investigation in the future. At the inflammatory stage, treatment with BGN@PTE substantially down-regulated a series of inflammatory cytokines, including TNF-α and IL-1β, and simultaneously ameliorated the oxidative stress and inflammatory microenvironment by scavenging ROS. On the other hand, our prepared BGN@PTE exhibited good antibacterial activity because of the multimodal synergistic antibacterial mechanisms of TA and EPL. *In vivo* treatment suggested that the application of BGN@PTE to mouse wounds had much more potent effects than BGN to prevent wound infection, reduce inflammation, and accelerate the healing process. Meanwhile, it was demonstrated that BGN@PTE possessed excellent bioactivities in promoting the migration of HUVECs *in vitro*. It has been confirmed that the SiO_4^{4-} within an appropriate concentration is a potent stimulator of angiogenesis that could promote the proliferation and migration of HUVECs and up-regulate the expression of angiogenesis-related genes, such as VEGF and basic fibroblast growth factor (bFGF) [49,50]. Notably, when compared with the control group, BGN, BGN@PT and

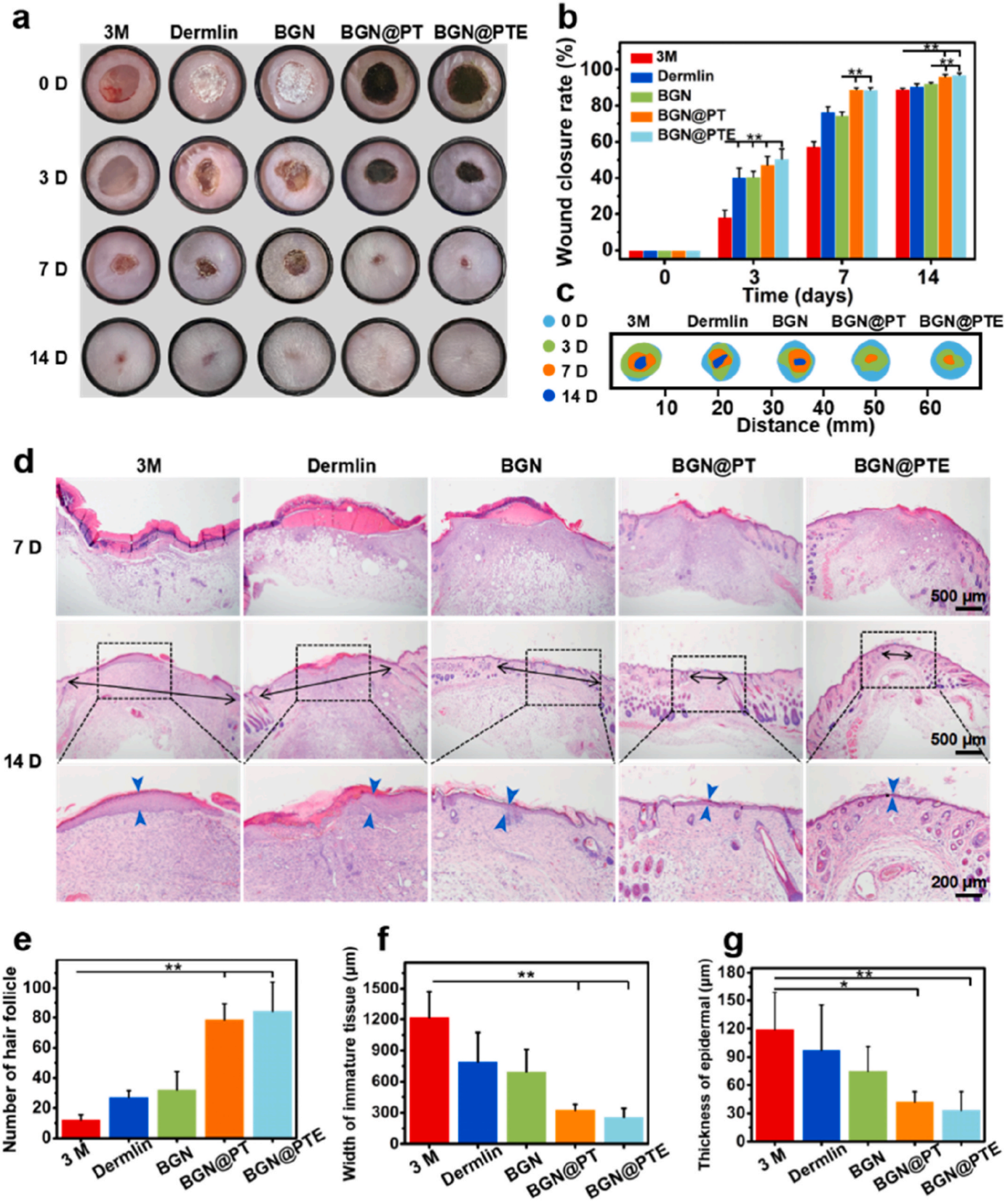

Fig. 5. BGN@PTE promoted wound repair and regeneration *in vivo*. (a) Representative images of the wounds in response to 3 M, Dermlin, BGN, BGN@PT, and BGN@PTE on days 0, 3, 7, and 14. (b) Quantitative analysis of wound healing rate for each group (n = 5, $^{**}p < 0.01$). (c) Schematic images of wound healing boundaries in different groups from day 0 to day 14. (d) H&E staining of wound tissues obtained from various groups on days 7 and 14 (n = 3, $^{*}p < 0.05$, $^{**}p < 0.01$, the immature tissue and epidermis are marked by black double arrow and blue arrow, respectively). Quantitative statistics of the number of hair follicle (e), width of immature tissue (f), and epidermal thickness (g) (n = 3, $^{*}p < 0.05$, $^{**}p < 0.01$).

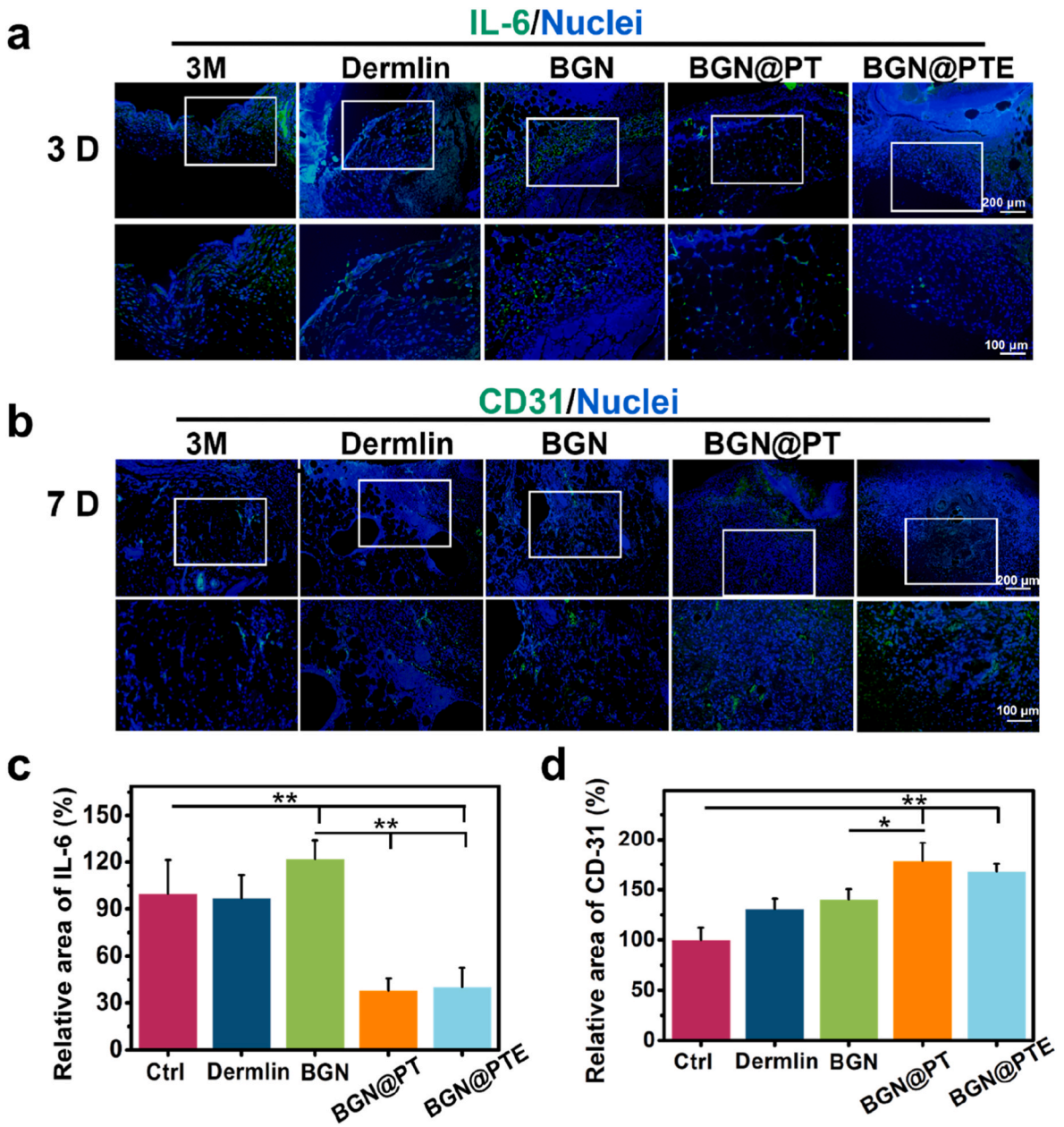

Fig. 6. Immunofluorescence staining analysis of wound healing *in vivo*. (a) Representative IL-6 immunofluorescence staining of wound tissues obtained from 3 M, Dermlin, BGN, BGN@PT, and BGN@PTE groups on day 3 (scale bar: 100 μm). (b) Representative CD31 immunofluorescence staining of the wound tissues obtained from each group on days 7 and 14 (scale bar: 100 μm). (c) The corresponding statistical results of IL-6 (n = 3, $^{*}p < 0.05$). (d) The corresponding statistical results of CD31 (n = 3, $^{*}p < 0.05$, $^{**}p < 0.01$).

BGN@PTE all exhibited the effect of up-regulating VEGF expression (Si concentration: 0.3–0.19 mg/L), with BGN@PTE being the most effective. To further explore the mechanism of BGN@PTE that promoted VEGF expression, BGN@PTE extracts were found to up-regulate the upstream factor HIF-1α level, resulting in enhanced VEGF expression *via* HIF-1α/VEGF cascade signaling in HUVECs. Therefore, the combination of BGN@PTE released bioactive ions and EPL showed a strong synergistic effect in stimulating angiogenesis. The wound closure rate on day 7 was used as an evaluation index in a mouse full-thickness wound model. We discussed and compared the different functional characteristics of the dressings such as Sr-doped BGN (BSr@PPE), quaternized chitosan/graphene oxide fabricated hydrogel (QCS-CD-AD/GO), poly (citrate-glycol-siloxane)/F127-ε-poly-L-lysine hybrid hydrogel (FEPCGS), Eu_2O_3 nanorods reinforced hydrogel (FHAE), photo-crosslinked CeO_2 hydrogel and EGCG-crosslinked chitosan hydrogel (EP) [51–56]. These results indicated that BGN@PTE provided significantly better wound healing performance than single antioxidant or angiogenic dressings (Fig. S14). The functional superiority of BGN@PTE endowed it with great potential for wound healing applications. Taken together, our work provides a feasible example for the preparation of multifunctional nanoplatforms by functionalizing BGN with polypeptides and polyphenols. More importantly, multilayer-structured BGN@PTE holds an extraordinary ability to manipulate the sequential healing of wounds from hemostasis to the inflammation phase and new tissue formation.

4. Conclusion

In summary, we successfully developed a multifunctional BGN@PTE dressing that not only achieved initial multi-pathway dependent rapid

hemostasis but also reconstructed the inflammatory infected wound microenvironment and accelerated wound healing processes. The layer-by-layer assembly of PTA and EPL endowed BGN with superior biocompatibility, unique hemostatic performance, and efficient anti-infection capability. Our study demonstrated that BGN, PTA and EPL showed a strong synergistic effect in treating intractable bleeding *in vitro* and *in vivo* by concentrating coagulating factors, improving tissue adhesion and activating the coagulation cascade. Meanwhile, the BGN@PTE powder could evenly cover irregular wounds for the treatment of full-thickness wound defects. Notably, BGN@PTE significantly reduced the inflammatory levels and oxidative stress and bacterial infection at wound sites, and stimulated cell migration and angiogenesis, thereby accelerating wound healing, which is superior to the result obtained with the commercial bioglass (Dermlin) dressing. It was expected that such BGN@PTE is a promising candidate for repairing wounds in multi-stage, and the incorporation of BGN with polyphenols and peptides might be an effective strategy for enhanced tissue regeneration.

CRediT authorship contribution statement

Yidan Wang: Investigation, Methodology, Data curation, Writing – original draft. **Meng luo:** Conceptualization, Methodology, Data curation. **Ting Li:** Conceptualization, Data curation, Formal analysis. **Chenxi Xie:** Methodology, Investigation. **Sihua Li:** Validation, Supervision, Funding acquisition. **Bo Lei:** Conceptualization, Project administration, Writing – review & editing.

Declaration of competing interest

All the authors declare that there's no financial/personal interest or belief that could affect their objectivity.

Acknowledgements

This work was supported by the Special Support Program for High Level Talents of Shaanxi Province of China, the key R&D plan of Shaanxi Province of China (grant No. 2021GXLH-Z-052), State Key Laboratory for Manufacturing Systems Engineering of China (grant No. sklms2021006), Young Talent Support Plan of Xi'an Jiaotong University of China (grant No. QY6J003).

Appendix A. Supplementary data

Supplementary data to this article can be found online at https://doi.org/10.1016/j.bioactmat.2023.01.019.

References

[1] M. Rodrigues, N. Kosaric, C.A. Bonham, G.C. Gurtner, Wound healing: a cellular perspective, Physiol. Rev. 99 (2019) 665–706.
[2] X. Ma, Y. Cheng, H. Jian, Y. Feng, Y. Chang, R. Zheng, X. Wu, L. Wang, X. Li, H. Zhang, Hollow, rough, and nitric oxide-releasing cerium oxide nanoparticles for promoting multiple stages of wound healing, Adv. Healthc. Mater. 8 (2019), 1900256.
[3] L. Lim, H. Bui, O. Farrelly, J. Yang, L. Li, D. Enis, W. Ma, M. Chen, G. Oliver, J. D. Welsh, M.L. Kahn, Hemostasis stimulates lymphangiogenesis through release and activation of VEGFC, Blood 134 (2019) 1764–1775.
[4] P. Heher, S. Muhleder, R. Mittermayr, H. Redl, P. Slezak, Fibrin-based delivery strategies for acute and chronic wound healing, Adv. Drug Deliv. Rev. 129 (2018) 134–147.
[5] A. Meddahi-Pelle, A. Legrand, A. Marcellan, L. Louedec, D. Letourneur, L. Leibler, Organ repair, hemostasis, and in vivo bonding of medical devices by aqueous solutions of nanoparticles, Angew. Chem. Int. Ed. 53 (2014) 6369–6373.
[6] Y.T. Wang, T. Ying, J.X. Li, Y.F. Xu, R.Q. Wang, Q.F. Ke, S.G.F. Shen, H. Xu, K. L. Lin, Hierarchical micro/nanofibrous scaffolds incorporated with curcumin and zinc ion eutectic metal organic frameworks for enhanced diabetic wound healing via anti-oxidant and anti-inflammatory activities, Chem. Eng. J. 402 (2020), 126273.
[7] H. Zhao, J. Huang, Y. Li, X.J. Lv, H.T. Zhou, H.R. Wang, Y.Y. Xu, C. Wang, J. Wang, Z. Liu, ROS-scavenging hydrogel to promote healing of bacteria infected diabetic wounds, Biomaterials 258 (2020), 120286.
[8] H.B. Wu, F.Y. Li, S.F. Wang, J.X. Lu, J.Q. Li, Y. Du, X.L. Sun, X.Y. Chen, J.Q. Gao, D. S. Ling, Ceria nanocrystals decorated mesoporous silica nanoparticle based ROS-scavenging tissue adhesive for highly efficient regenerative wound healing, Biomaterials 151 (2018) 66–77.
[9] C.Y. Chen, H. Yin, X. Chen, T.H. Chen, H.M. Liu, S.S. Rao, Y.J. Tan, Y.X. Qian, Y. W. Liu, X.K. Hu, M.J. Luo, Z.X. Wang, Z.Z. Liu, J. Cao, Z.H. He, B. Wu, T. Yue, Y. Y. Wang, K. Xia, Z.W. Luo, Y. Wang, W.Y. Situ, W.E. Liu, S.Y. Tang, H. Xie, Angstrom-scale silver particle-embedded carbomer gel promotes wound healing by inhibiting bacterial colonization and inflammation, Sci. Adv. 6 (2020), 0942.
[10] Y.M. Xiang, C.Y. Mao, X.M. Liu, Z.D. Cui, D.D. Jing, X.J. Yang, Y.Q. Liang, Z.Y. Li, S.L. Zhu, Y.F. Zheng, K.W.K. Yeung, D. Zheng, X.B. Wang, S.L. Wu, Rapid and superior bacteria killing of carbon quantum dots/ZnO decorated injectable folic acid-conjugated PDA hydrogel through dual-light triggered ros and membrane permeability, Small 15 (2019), 1900322.
[11] Z.L. Tu, M. Chen, M. Wang, Z.X. Shao, X.Q. Jiang, K.Y. Wang, Z. Yao, S.W. Yang, X. X. Zhang, W.Y. Gao, C. Lin, B. Lei, C. Mao, Engineering bioactive M2 macrophage-polarized anti-inflammatory, antioxidant, and antibacterial scaffolds for rapid angiogenesis and diabetic wound repair, Adv. Funct. Mater. 31 (2021), 2100924.
[12] S. Hamdan, I. Pastar, S. Drakulich, E. Dikici, M. Tomic-Canic, S. Deo, S. Daunert, Nanotechnology-driven therapeutic interventions in wound healing: potential uses and applications, ACS Cent. Sci. 3 (2017) 163–175.
[13] F.L. Tang, J.L. Li, W.H. Xie, Y.F. Mo, L. Ouyang, F.J. Zhao, X.L. Fu, X.F. Chen, Bioactive glass promotes the barrier functional behaviors of keratinocytes and improves the Re-epithelialization in wound healing in diabetic rats, Bioact. Mater. 6 (2021) 3496–3506.
[14] Y.L. Zhu, Z.J. Ma, L.Z. Kong, Y.H. He, H.F. Chan, H.Y. Li, Modulation of macrophages by bioactive glass/sodium alginate hydrogel is crucial in skin regeneration enhancement, Biomaterials 256 (2020), 120216.
[15] T.H. Kim, M.S. Kang, N. Mandakhbayar, A. El-Fiqi, H.W. Kim, Anti-inflammatory actions of folate-functionalized bioactive ion-releasing nanoparticles imply drug-free nanotherapy of inflamed tissues, Biomaterials 207 (2019) 23–38.
[16] Y.L. Zhou, C.T. Wu, J. Chang, Bioceramics to regulate stem cells and their microenvironment for tissue regeneration, Mater, Today Off. 24 (2019) 41–56.
[17] M. Schumacher, P. Habibovic, S. van Rijt, Mesoporous bioactive glass composition effects on degradation and bioactivity, Bioact. Mater. 6 (2021) 1921–1931.
[18] L.Z. Kong, Z. Wu, H.K. Zhao, H.M. Cui, J. Shen, J. Chang, H.Y. Li, Y.H. He, Bioactive injectable hydrogels containing desferrioxamine and bioglass for diabetic wound healing, ACS Appl. Mater. Interfaces 10 (2018) 30103–30114.
[19] Y. Xu, J.L. Peng, X. Dong, Y.H. Xu, H.Y. Li, J. Chang, Combined chemical and structural signals of biomaterials synergistically activate cell-cell communications for improving tissue regeneration, Acta Biomater. 55 (2017) 249–261.
[20] T.A. Ostomel, Q.H. Shi, G.D. Stucky, Oxide hemostatic activity, J. Am. Chem. Soc. 128 (2006) 8384–8385.
[21] V. Miguez-Pacheco, L.L. Hench, A.R. Boccaccini, Bioactive glasses beyond bone and teeth: emerging applications in contact with soft tissues, Acta Biomater. 13 (2015) 1–15.
[22] E. Sharifi, A. Bigham, S. Yousefiasl, M. Trovato, M. Ghomi, Y. Esmaeili, P. Samadi, A. Zarrabi, M. Ashrafizadeh, S. Sharifi, R. Sartorius, F.D. Moghaddam, A. Maleki, H. Song, T. Agarwal, T.K. Maiti, N. Nikfarjam, C. Burvill, V. Mattoli, M.G. Raucci, K. Zheng, A.R. Boccaccini, L. Ambrosio, P. Makvandi, Mesoporous bioactive glasses in cancer diagnosis and therapy: stimuli-responsive, toxicity, immunogenicity, and clinical translation, Adv. Sci. 9 (2022), 2102678.
[23] W. Niu, Y. Guo, Y.M. Xue, M. Wang, M. Chen, D.D. Winston, W. Cheng, B. Lei, Biodegradable multifunctional bioactive Eu-Gd-Si-Ca glass nanoplatform for integrative imaging-targeted tumor therapy-recurrence inhibition-tissue repair, Nano Today 38 (2021), 101137.
[24] M. Chen, M. Wang, W. Niu, W. Cheng, Y. Guo, Y.D. Wang, M. Luo, C.X. Xie, T. T. Leng, X.X. Zhang, C. Lin, B. Lei, Multifunctional protein-decorated bioactive glass nanoparticles for tumor-specific therapy and bioimaging *in vitro* and *in vivo*, ACS Appl. Mater. Interfaces 13 (2021) 14985–14994.
[25] X.Q. Zhang, Z. Li, P. Yang, G.G. Duan, X.H. Liu, Z.P. Gu, Y.W. Li, Polyphenol scaffolds in tissue engineering, Mater. Horiz. 8 (2021) 145.
[26] W.Z. Qiu, G.P. Wu, Z.K. Xu, Robust coatings via catechol-amine codeposition: mechanism, kinetics, and application, ACS Appl. Mater. Interfaces 10 (2018) 5902–5908.
[27] J.I. Clodt, V. Filiz, S. Rangou, K. Buhr, C. Abetz, D. Höche, J. Hahn, A. Jung, V. Abetz, Double stimuli-responsive isoporous membranes via post-modification of ph-sensitive self-assembled diblock copolymer membranes, Adv. Funct. Mater. 23 (2013) 731–738.
[28] S.M. Bai, X.L. Zhang, X.L. Lv, M.Y. Zhang, X.W. Huang, Y. Shi, C.H. Lu, J.B. Song, H.H. Yang, Bioinspired mineral-organic bone adhesives for stable fracture fixation and accelerated bone regeneration, Adv. Funct. Mater. 30 (2020), 1908381.
[29] X. Su, Y. Luo, Z.L. Tian, Z.Y. Yuan, Y.M. Han, R.F. Dong, L. Xu, Y.T. Feng, X.Z. Liu, J.Y. Huang, Ctenophore-inspired hydrogels for efficient and repeatable underwater specific adhesion to biotic surfaces, Mater. Horiz. 7 (2020) 2651–2661.
[30] J.W. Chen, L.P. Qiu, Q.L. Li, J. Ai, H.Q. Liu, Q.H. Chen, Rapid hemostasis accompanied by antibacterial action of calcium crosslinking tannic acid-coated mesoporous silica/silver Janus nanoparticles, Mater. Sci. Eng. C 123 (2021), 111958.
[31] C.W. Wang, H.Y. Zhou, H.Y. Niu, X.Y. Ma, Y. Yuan, H. Hong, C.S. Liu, Tannic acid-loaded mesoporous silica for rapid hemostasis and antibacterial activity, Biomater. Sci. 6 (2018) 3318.

[32] D.A. Hickman, C.L. Pawlowski, U.D.S. Sekhon, J. Marks, A. Gupta, Biomaterials and advanced technologies for hemostatic management of bleeding, Adv. Mater. 30 (2018), 1700859.
[33] M. Yu, Y.M. Xue, P.X. Ma, C. Mao, B. Lei, Intrinsic ultrahigh drug/mirna loading capacity of biodegradable bioactive glass nanoparticles toward highly efficient pharmaceutical delivery, ACS Appl. Mater. Interfaces 9 (2017) 8460–8470.
[34] J.Y. Liu, Y. Hu, L. Li, C. Wang, J. Wang, Y. Li, D.F. Chen, X.K. Ding, C.A. Shen, F. J. Xu, Biomass-derived multilayer-structured microparticles for accelerated hemostasis and bone repair, Adv. Sci. 7 (2020), 2002243.
[35] T. Saotome, H. Hayashi, R. Tanaka, A. Kinugasa, S. i Uesugi, K. Tatematsu, H. Sezutsu, N. Kuwabara, T. Asakura, Introduction of VEGF or RGD sequences improves revascularization properties of Bombyx mori silk fibroin produced by transgenic silkworm, J. Mater. Chem. B 3 (2015) 7109.
[36] S.M. Andrabi, S. Majumder, K.C. Gupta, A. Kumar, Dextran based amphiphilic nano-hybrid hydrogel system incorporated with curcumin and cerium oxide nanoparticles for wound healing, Colloids Surf., B 195 (2020), 111236.
[37] Q. Li, E.L. Hu, K. Yu, R.Q. Xie, F. Lu, B.T. Lu, R. Bao, T.F. Zhao, F.Y. Dai, G.Q. Lan, Self-propelling janus particles for hemostasis in perforating and irregular wounds with massive hemorrhage, Adv. Funct. Mater. 30 (2020), 2004253.
[38] S.S. Yang, J.L. Ji, M.W. Luo, H.L. Li, Z.H. Gao, Poly(tannic acid) nanocoating based surface modification for construction of multifunctional composite CeO_2NZs to enhance cell proliferation and antioxidative viability of preosteoblasts, Nanoscale 13 (2021) 16349–16361.
[39] C.B. Yuan, Y. Zhang, J.S. Yao, Q.Z. Liu, F.G. Kong, Facile synthesis of polyethylene glycol@tannin-amine microsphere towards cr(vi) removal, Polymers 13 (2021) 1035.
[40] H. Qiu, Q.F. Tu, P. Gao, X.Y. Li, M.F. Maitz, K.Q. Xiong, N. Huang, Z.L. Yang, Phenolic-amine chemistry mediated synergistic modification with polyphenols and thrombin inhibitor for combating the thrombosis and inflammation of cardiovascular stents, Biomaterials 269 (2021), 120626.
[41] W.G. Wang, J.K. Sun, Y.Q. Zhang, Y. Zhang, G.H. Hong, R.M. Moutloali, B. B. Mamba, F.R. Li, J. Ma, L. Shao, Mussel-inspired tannic acid/polyethyleneimine assembling positively-charged membranes with excellent cation permselectivity, Sci. Total Environ. 817 (2022), 153051.
[42] S.H. Zhang, Z.Y. Jiang, X.L. Wang, C. Yang, J.F. Shi, Facile method to prepare microcapsules inspired by polyphenol chemistry for efficient enzyme immobilization, ACS Appl. Mater. Interfaces 7 (2015) 19570–19578.
[43] B. Alcalde, M. Granados, J. Saurina, Exploring the antioxidant features of polyphenols by spectroscopic and electrochemical methods, Antioxidants 8 (2019) 523.
[44] S. Pourshahrestani, N.A. Kadri, E. Zeimaran, M.R. Towler, Well-ordered mesoporous silica and bioactive glasses: promise for improved hemostasis, Biomater. Sci. 7 (2019) 31–50.
[45] A. Shahidullah, J.Y. Lee, Y.J. Kim, S.M.A. Halimi, A. Rauf, H.J. Kim, B.Y. Kim, W. Park, Anti-Inflammatory effects of diospyrin on lipopolysaccharide-induced inflammation using RAW 264.7 mouse macrophages, Biomedicines 8 (2020) 11.
[46] A.S. Glaive, T. Modjinou, D.L. Versace, S. Abbad-Andaloussi, P. Dubot, V. Langlois, E. Renard, Design of antibacterial and sustainable antioxidant networks based on plant phenolic derivatives used as delivery system of carvacrol or tannic acid, ACS Sustain. Chem. Eng. 5 (2017) 2320–2329.
[47] C.E. Hansen, Y.Z. Qiu, O.J.T. McCarty, W.A. Lam, Platelet mechanotransduction, Annu. Rev. Biomed. Eng. 20 (2018) 253–275.
[48] Y.C. Guo, Y. Wang, X.H. Zhao, X. Li, Q. Wang, W. Zhong, K. Mequanint, R.X. Zhan, M. Xing, G.X. Luo, Snake extract-laden hemostatic bioadhesive gel cross-linked by visible light, Sci. Adv. 7 (2021) 9635.
[49] Q.Q. Yu, J. Chang, C.T. Wu, Silicate bioceramics: from soft tissue regeneration to tumor therapy, J. Mater. Chem. B 7 (2019) 5449–5460.
[50] S. Kargozar, F. Baino, S. Hamzehlou, R.G. Hill, M. Mozafari, Bioactive glasses: sprouting angiogenesis in tissue engineering, Trends Biotechnol. 36 (2018) 430–444.
[51] M. Chen, D.D. Winston, M. Wang, W. Niu, W. Cheng, Y. Guo, Y.D. Wang, M. Luo, C. X. Xie, T.T. Leng, X.T. Qu, B. Lei, Hierarchically multifunctional bioactive nanoglass for integrated tumor/infection therapy and impaired wound repair, Mater. Today 53 (2022) 27–40.
[52] B.L. Zhang, J.H. He, M.T. Shi, Y.Q. Liang, B.L. Guo, Injectable self-healing supramolecular hydrogels with conductivity and photo-thermal antibacterial activity to enhance complete skin regeneration, Chem. Eng. J. 400 (2020), 125994.
[53] W. Cheng, M. Wang, M. Chen, W. Niu, Y.N. Li, Y.D. Wang, M. Luo, C.X. Xie, T. T. Leng, B. Lei, Injectable antibacterial antiinflammatory molecular hybrid hydrogel dressing for rapid MDRB-infected wound repair and therapy, Chem. Eng. J. 409 (2021), 128140.
[54] M. Luo, M. Wang, W. Niu, M. Chen, W. Cheng, L. Zhang, C.X. Xie, Y.D. Wang, Y. Guo, T.T. Leng, X. X Zhang, C. Lin, B. Lei, Injectable self-healing anti-inflammatory europium oxide-based dressing with high angiogenesis for improving wound healing and skin regeneration, Chem. Eng. J. 412 (2021), 128471.
[55] Z.M. Yang, X.H. Ren, Y. Liu, N-halamine modified ceria nanoparticles: antibacterial response and accelerated wound healing application via a 3D printed scaffold, Composites Part B 227 (2021), 109390.
[56] Q.C. Wei, L. Ma, W.W. Zhang, G.L. Ma, Z.G. Hu, EGCG-crosslinked carboxymethyl chitosan-based hydrogels with inherent desired functions for fullthickness skin wound healing, J. Mater. Chem. B 10 (2022) 3927.